

Direct Numerical Simulation Code Validation for Compressible Shear Flows Using Linear Stability Theory

Jônatas Ferreira Lacerda¹, Leandro Franco de Souza¹, Josuel Kruppa Rogenski¹, Márcio Teixeira de Mendonça²

How to cite:

Lacerda JF  <https://orcid.org/0000-0001-5147-5127>

Souza LF  <https://orcid.org/0000-0002-6145-9443>

Rogenski JK  <https://orcid.org/0000-0002-3364-3593>

Mendonça MT  <https://orcid.org/0000-0002-6630-0749>

Lacerda JF, Souza LF, Rogenski JK, Mendonça MT (2018) Direct numerical simulation code validation for compressible shear flows using linear stability theory. J Aerosp Technol Manag, 10: e2318. doi: 10.5028/jatm.v10.858

ABSTRACT: In order to simulate compressible shear flow stability and aeroacoustic problems, a numerical code must be able to capture how a baseflow behaves when submitted to small disturbances. If the disturbances are amplified, the flow is unstable. The linear stability theory (LST) provides a framework to obtain information about the growth rate in relation to the excitation frequency for a given baseflow. A linear direct numerical simulation (DNS) should capture the same growth rate as the LST, providing a severe test for the code. In the present study, DNS simulations of a two-dimensional compressible mixing layer and of a two-dimensional compressible plane jet are performed. Disturbances are introduced at the domain inflow and spatial growth rates obtained with a DNS code are compared with growth rates obtained from LST analyses, for each baseflow, in order to verify and validate the DNS code. The good comparison between DNS simulations and LST results indicates that the code is able to simulate compressible flow problems and it is possible to use it to perform numerical simulation of instability and aeroacoustic problems.

KEYWORDS: Compressible flow, Direct numerical simulation, Linear stability theory, Code verification and validation.

INTRODUCTION

There is an increasing concern about noise-related health problems in many engineering areas. Some noise sources are due to turbulence in a flow field and aeroacoustics is the area responsible for the investigation of noise generation and propagation (aerodynamic noise). The problem of noise generated by flow has some specific characteristics, such as multiple frequencies, multiple scales and propagation to long distances with very low dissipation (Tam 2004). To deal with these characteristics, a numerical simulation must have a transient numerical scheme, very low numerical dissipation and dispersion to preserve the propagation of acoustic waves and non-reflecting boundary conditions (Tam 2004).

Two main strategies are frequently used to simulate aeroacoustic problems. The first one is based on acoustic analogies (Lighthill 1952; Lighthill 1954; Curle 1955; Ffowcs-Williams and Hawkins 1969), where noise sources are obtained from computational fluid dynamics (CFD) and its propagation is calculated solving an inhomogeneous wave equation for pressure, subjected to these

1. Universidade de São Paulo – Instituto de Ciências Matemáticas e de Computação – Departamento de Matemática Aplicada e Estatística – São Carlos/SP – Brazil.
2. Departamento de Ciência e Tecnologia Aeroespacial – Instituto de Aeronáutica e Espaço – Divisão de Propulsão Aeronáutica – São José dos Campos/SP – Brazil.

Correspondence author: Leandro Franco de Souza | Universidade de São Paulo Instituto de Ciências Matemáticas e de Computação – Departamento de Matemática Aplicada e Estatística | Av. do Trabalhador São-Carlense, 400 – Centro | Cx. Postal: 668, CEP: 13560-970 – São Carlos/SP – Brazil | E-mail: lefraso@icmc.usp.br

Received: Dec. 12, 2016 | Accepted: Jun. 06, 2017

Section Editor: John Cater



sources. The second approach uses a high fidelity simulation capable of computing directly the acoustic waves together with the fluid flow, which is called direct aeroacoustic simulation.

In order to perform direct aeroacoustic simulation, a numerical code was developed within our research group (Souza *et al.* 2005). It uses parallel processing with domain decomposition to perform the calculations in a feasible time. High order temporal and spatial discretization schemes were adopted to minimize the dispersion and dissipation phenomena on the simulation of the flow field and the acoustic waves. A series of strategies, such as filtering and mesh stretching as well as characteristic boundary conditions were implemented in order to obtain a proper solution of the aeroacoustic problems.

However, before using a direct numerical simulation (DNS) code for aeroacoustic predictions, it is a good practice to observe the code behavior when submitted to unsteady, small disturbances. The linear stability theory (LST) provides a framework to obtain information about the amplification rate in relation to the excitation frequency and corresponding eigenfunctions. The results from LST can then be used for comparison with numerical simulations.

In the present study, results are presented for DNS of a two-dimensional compressible mixing layer and two-dimensional compressible plane jet. Disturbances were introduced at the domain inflow and the code verification was done by comparing the spatial amplification rate obtained by the DNS code with the amplification rates obtained from a LST analysis of each baseflow. The good comparison obtained indicated that the code satisfactorily simulates compressible flow problems and can be used to perform direct aeroacoustic simulations.

FORMULATION AND NUMERICAL SCHEME

The code was developed to solve the two-dimensional unsteady compressible Navier-Stokes equations together with the continuity and energy equations in dimensionless form. A Cartesian reference frame (x, y) was adopted, where the x axis is aligned with the streamwise direction and the y axis with the normal direction. The corresponding velocity components are u and v . In conservative form, the solution vector is given by:

$$\mathbf{Q} = (\rho, \rho u, \rho v, E)^T. \quad (1)$$

A perfect gas relation for pressure is assumed to close the formulation. In the conservative form, the unknowns are the density ρ , the momentum densities ρu , ρv and the total energy E , given by:

$$E = \rho \int c_v dT + \frac{\rho}{2} (u^2 + v^2), \quad (2)$$

where c_v is the specific heat at constant volume and T is the temperature. All equations can be written in vector notation as:

$$\frac{\partial \mathbf{Q}}{\partial t} + \frac{\partial \mathbf{F}}{\partial x} + \frac{\partial \mathbf{G}}{\partial y} = 0, \quad (3)$$

where the flux vectors \mathbf{F} and \mathbf{G} are given by:

$$\mathbf{F} = \begin{bmatrix} \rho u \\ \rho u u + p - \tau_{xx} \\ \rho u v - \tau_{xy} \\ u(E + p) + q_x - u\tau_{xx} - v\tau_{xy} \end{bmatrix}, \quad (4)$$

$$\mathbf{G} = \begin{bmatrix} \rho v \\ \rho v u - \tau_{xy} \\ \rho v v + p - \tau_{yy} \\ v(E + p) + q_y - u\tau_{xy} - v\tau_{yy} \end{bmatrix}, \quad (5)$$

where p is the normalized pressure. The normal stress components are given by:

$$\tau_{xx} = \frac{\mu}{\text{Re}} \left(\frac{4}{3} \frac{\partial u}{\partial x} - \frac{2}{3} \frac{\partial v}{\partial y} \right), \quad (6)$$

$$\tau_{yy} = \frac{\mu}{\text{Re}} \left(\frac{4}{3} \frac{\partial v}{\partial y} - \frac{2}{3} \frac{\partial u}{\partial x} \right), \quad (7)$$

and the shear stress component is:

$$\tau_{xy} = \frac{\mu}{\text{Re}} \left(\frac{\partial u}{\partial y} + \frac{\partial v}{\partial x} \right). \quad (8)$$

The heat fluxes, considering the Fourier law for heat conduction, are given by:

$$q_x = - \frac{\vartheta}{(\kappa - 1) \text{Re Pr Ma}_\infty^2} \frac{\partial T}{\partial x}, \quad (9)$$

$$q_y = - \frac{\vartheta}{(\kappa - 1) \text{Re Pr Ma}_\infty^2} \frac{\partial T}{\partial y}. \quad (10)$$

The dimensionless quantities are the Reynolds number Re , the Prandtl number Pr and the Mach number Ma . The dimensionless fluid properties are the viscosity μ , the thermal conductivity ϑ and the heat capacity ratio κ . All fluid properties are normalized by reference velocity \tilde{u}_∞ , temperature \tilde{T}_∞ , density $\tilde{\rho}_\infty$, and viscosity $\tilde{\mu}_\infty$, where the superscript \sim represents dimensional values and the subscript ∞ corresponding to free-stream values.

Time integration is performed using a 4th order, 4-steps Runge-Kutta scheme. Spatial discretization in the streamwise x and normal y directions uses a 6th order compact finite difference method and the generated tridiagonal equation systems are solved using the Thomas algorithm.

A non-uniform grid is used. An interest region with uniform grid is delimited. Then a grid stretching of approximately 1% is applied in both directions that, together with spatial low-pass filtering, create a damping zone. Disturbances become increasingly badly resolved and are dissipated as they propagate through the damping zone before they reach the outflow boundaries.

The code was parallelized through domain decomposition in both directions using distributed-memory parallelization. A message passing interface (MPI) library is used for inter-node communications. A grid transformation in the (x, y) plane is used to map the physical grid in an equidistant (ξ, η) computational grid. The metrics required for the derivative calculations are presented below. The first derivatives are given by:

$$\frac{\partial}{\partial x} = \frac{1}{\begin{pmatrix} \frac{\partial x}{\partial \xi} \\ \frac{\partial \xi}{\partial x} \end{pmatrix}} \frac{\partial}{\partial \xi}, \quad (11)$$

$$\frac{\partial}{\partial y} = \frac{1}{\left(\frac{\partial y}{\partial \eta}\right)} \frac{\partial}{\partial \eta} . \quad (12)$$

Second derivatives are:

$$\frac{\partial^2}{\partial x^2} = \frac{\partial^2}{\partial \xi^2} \left(\frac{\partial \xi}{\partial x}\right)^2 - \frac{\partial}{\partial \xi} \frac{\partial^2 \xi}{\partial x^2} , \quad (13)$$

$$\frac{\partial^2}{\partial y^2} = \frac{\partial^2}{\partial \eta^2} \left(\frac{\partial \eta}{\partial y}\right)^2 - \frac{\partial}{\partial \eta} \frac{\partial^2 \eta}{\partial y^2} , \quad (14)$$

where the metrics are given by:

$$\frac{\partial^2 \xi}{\partial x^2} = -\frac{\partial^2 x}{\partial \xi^2} \left(\frac{\partial \xi}{\partial x}\right)^3 , \quad (15)$$

$$\frac{\partial^2 \eta}{\partial y^2} = -\frac{\partial^2 y}{\partial \eta^2} \left(\frac{\partial \eta}{\partial y}\right)^3 . \quad (16)$$

LST analysis was used to obtain the frequency with spatial growth rate and the corresponding eigenfunctions are introduced as disturbances at the simulation inflow boundary.

RESULTS AND DISCUSSIONS

COMPRESSIBLE TWO-DIMENSIONAL MIXING LAYER

A compressible mixing layer consists of two streams with different velocities flowing parallel to one another, so that the resulting streamwise velocity profile assumes an “S” shape. Due to the inflectional point on the velocity profile, the flow is unstable and transition to turbulence may occur due to the generation and growth of vortical structures. For the present verification, the flow configuration has been closely matched to the case investigated by Babucke *et al.* (2008).

The Mach numbers of the upper and lower streams are $Ma_1 = 0.50$ and $Ma_2 = 0.25$, respectively. The Reynolds number is 500, based on the vorticity thickness at the inflow, which is also used to normalize length scales in x and y directions. As in Babucke *et al.* 2008, the inflow ($x_0 = 30$) is chosen in such a way that the vorticity thickness is:

$$\delta(x_0 = 30) = \left(\frac{\Delta U}{|\partial u / \partial y|_{\max}} \right)_{x_0=30} = 1.0. \quad (17)$$

The inflow streamwise velocity, density and temperature profiles are shown in Fig. 1. These profiles are obtained by solving the steady compressible two-dimensional boundary layer equations.

The eigenfunctions used to introduce the disturbances at the DNS inflow boundary were obtained by linear stability analysis. The dimensionless fundamental frequency is $\omega = 0.62930$. The corresponding eigenfunction amplitude and phase are shown in Fig. 2. This frequency and three subharmonics were used to disturb the flow. The maximum amplitude of the dimensionless fundamental frequency is 2×10^{-3} , while for the other subharmonics the maximum amplitude is 1×10^{-3} . All amplitudes are normalized by the corresponding maximum streamwise velocity amplitude. Furthermore, a phase shift of $\Delta\theta = -0.028$ was introduced for the first subharmonic, $\Delta\theta = -0.141$ for the second and $\Delta\theta = -0.391$ for the third, as used by Babucke *et al.* (2008).

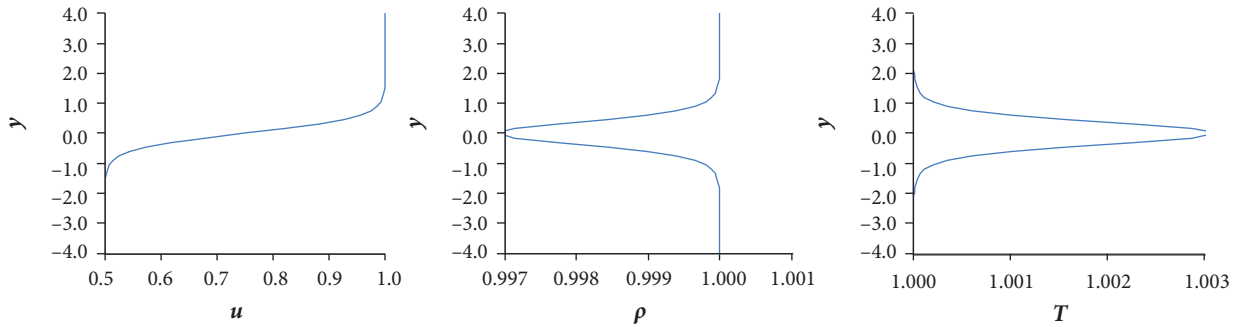


Figure 1. Inflow profiles for u , ρ and T for the 2D mixing layer.

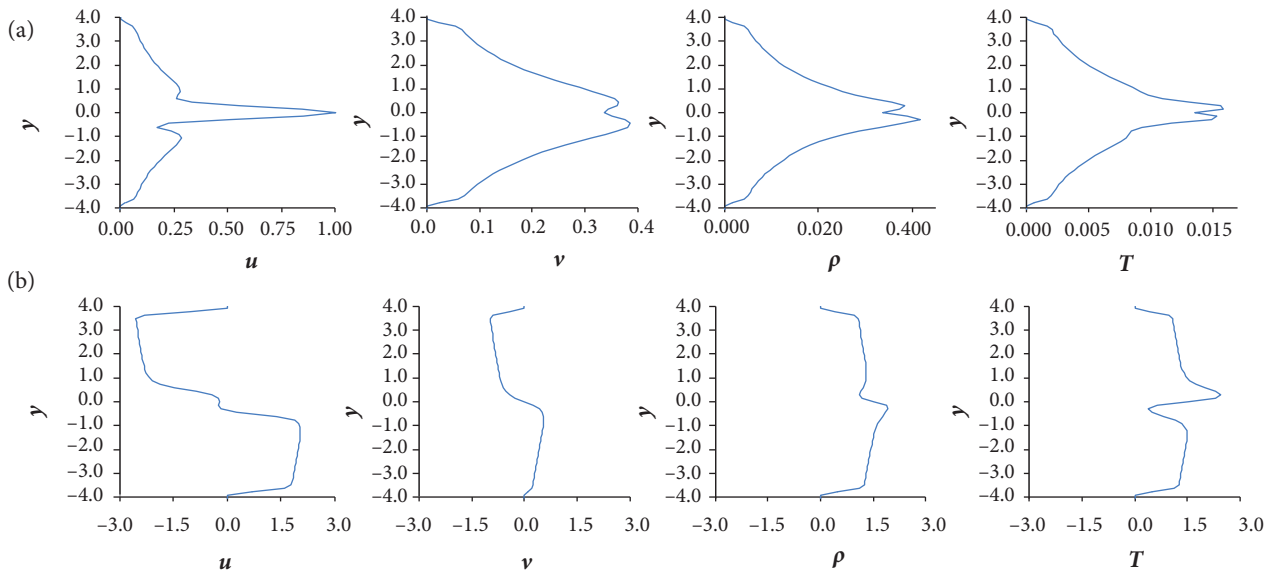


Figure 2. (a) Amplitude and (b) phase distribution for the 2D mixing layer.

The computational mesh, with 2500×850 points in the x and y directions, respectively, is presented in Fig. 3, showing the domain regions and boundary conditions. In the longitudinal direction, the mesh has constant increment $\Delta x = 0.157$ up to $x = 300$, forming the region of interest. Further downstream, the mesh is stretched with a rate of approximately 1.0%, forming a damping zone. In the normal direction, the mesh is stretched from the center to the boundaries, with the lowest increment of $\Delta y = -0.15$ and the highest increment of $\Delta y = 1.06$. Tests with a coarse and finer mesh indicate that the adopted mesh is suitable for the simulations carried out here.

At the inflow, the undisturbed boundary conditions were defined by a null v velocity; the u velocity, temperature and density profiles are presented in Fig. 1. The total energy E is calculated by Eq. 2. The disturbances were introduced at each time step of the Runge-Kutta method. Furthermore, characteristic boundary conditions are used at the inflow to avoid outgoing wave reflections back to the computational domain. The characteristic variable c , which corresponds to the outgoing waves at the inflow boundary, can be obtained from the baseflow and flow fluctuations by:

$$c = -u' \rho_0 a_0 + p', \tag{18}$$

where the subscript 0 represents the baseflow variables, superscript ' represents the flow fluctuations and a_0 is the speed of sound at the freestream. The characteristics can be calculated from regions in the flow domain that are close to the inflow boundary

and extrapolated to it by:

$$c_{(j=1)} = 3 \cdot c_{(j=2)} - 3 \cdot c_{(j=3)} + c_{(j=4)}. \quad (19)$$

Once $c_{(j=1)}$ is calculated, the flow fluctuations at the inflow boundary can be calculated as:

$$\begin{cases} \rho' = c/2a_0^2, \\ u' = c/2\rho_0 a_0^2, \\ v' = 0, \\ p' = c/2. \end{cases} \quad (20)$$

and these values are added to the inflow boundary variables.

To minimize reflections at the freestream (upper and lower boundary) and at the outflow boundaries, caused by normal and oblique acoustic waves (Babucke *et al.* 2008), a combination of grid stretching and spatial low-pass filtering is applied in the damping zone, forcing the flow variables to a steady-state solution. Thus, the disturbances become increasingly badly resolved as they propagate through this region and by applying a spatial filter, the perturbations are substantially dissipated before they reach the boundaries. The computational domain was decomposed into 2 parts in the y direction and 7 parts in the x direction, adopting 14 processing elements to perform the calculations.

The chosen time step was $\Delta t = 2\pi/\omega \cdot n_{\text{steps}}$, where n_{steps} is the number of points per wavelength of the fundamental frequency. In the present case $n_{\text{steps}} = 752$ was adopted, corresponding to a time step of $\Delta t = 1.33 \times 10^{-2}$. Seventy-six periods of the fundamental frequency were simulated and the last eight were chosen for post-processing analysis. By considering 76 periods, we ensure that the results are free of numerical transients.

The maximum amplitude of the normal velocity component v , for each streamwise x position, shows how the disturbances behave (Fig. 4). In the initial part of the domain, the amplitudes grow exponentially until non-linear effects are observed, causing a saturation of the maximum amplitude of v .

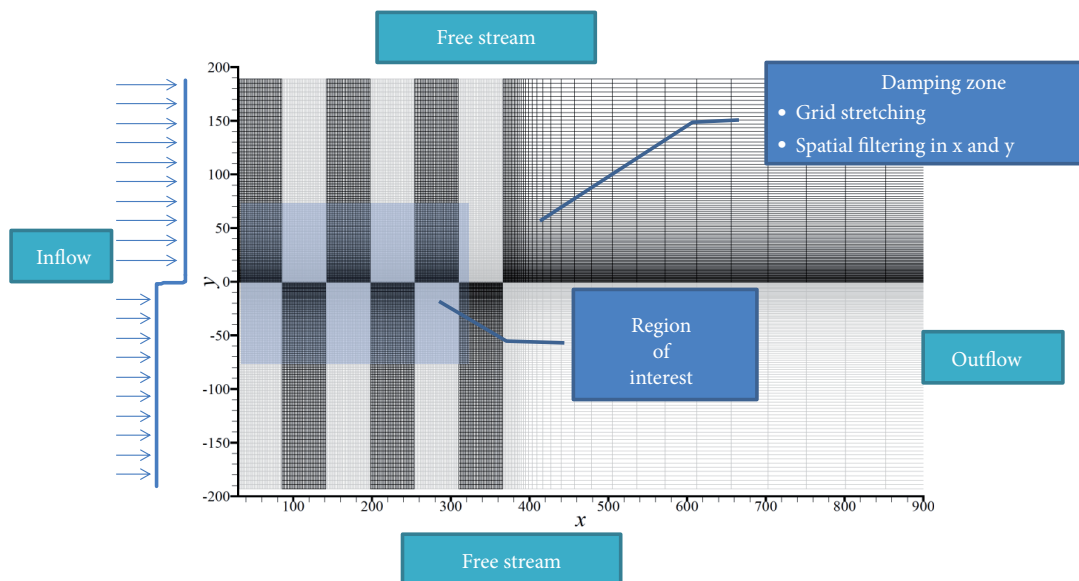


Figure 3. Computational domain highlighting the region of interest, the damping zone and the boundaries for 2D mixing layer.

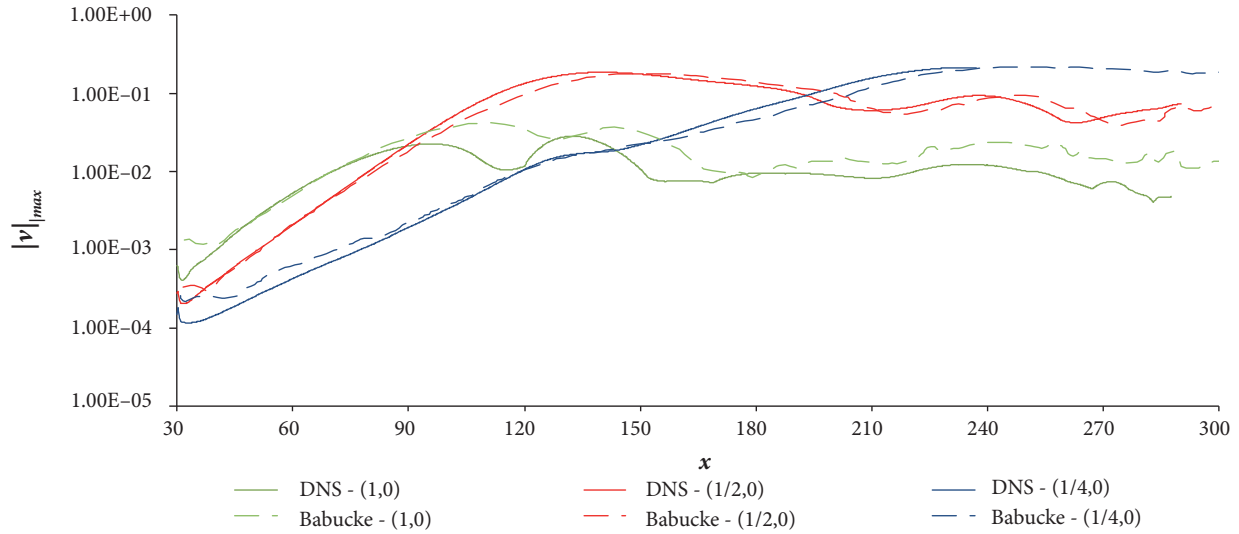


Figure 4. Maximum amplitude of v for each x position. Comparison with results from Babucke *et al.* (2008).

The spatial growth rate α_i is calculated by Eq. 21. It can be compared with results from LST, as shown in Fig. 5. Table 1 presents the difference between DNS and LST results, where there is an initial portion of the domain with large error due to the receptivity region. Further downstream, where the transient of all three modes has vanished, the differences decrease as shown in Table 1. Although α_i is a very sensitive value, mainly for the subharmonics, the mean values of the DNS corresponded well to those predicted by LST. Thus, the good agreement between simulation and LST serves as verification of the implemented DNS computational code for small disturbances propagation.

$$\alpha_i = -\frac{\partial}{\partial x} \left[\ln(|v|_{\max}) \right]. \tag{21}$$

Besides the spatial amplification rate comparison, the spanwise vorticity Ω_z was compared with the results presented by Babucke *et al.* (2008), as shown in Fig. 6. It is possible to see the formation of the first Kelvin-Helmholtz vortices which will pair with neighboring ones to form new structures downstream. A good qualitative agreement was observed.

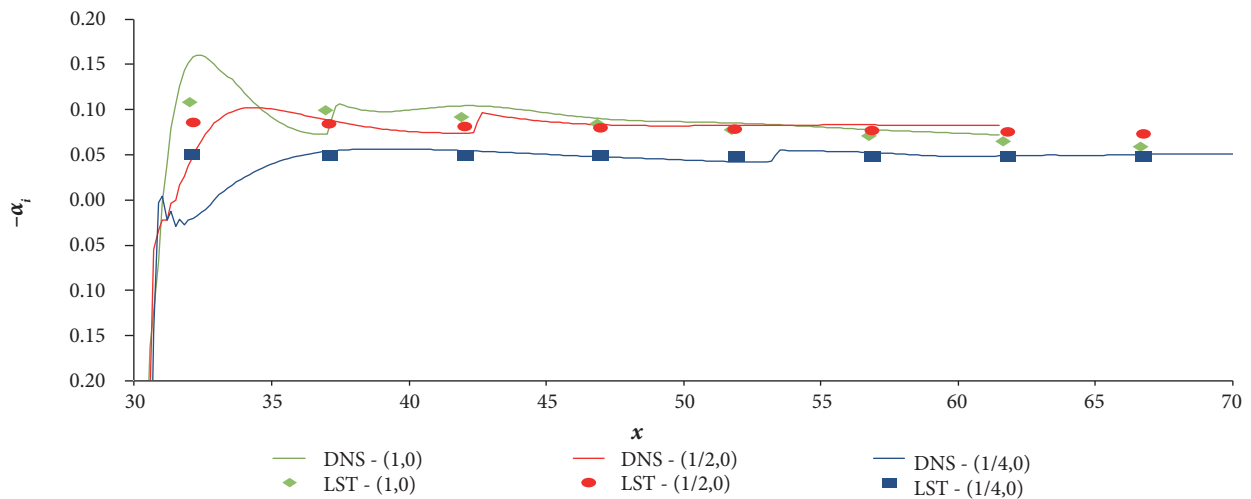
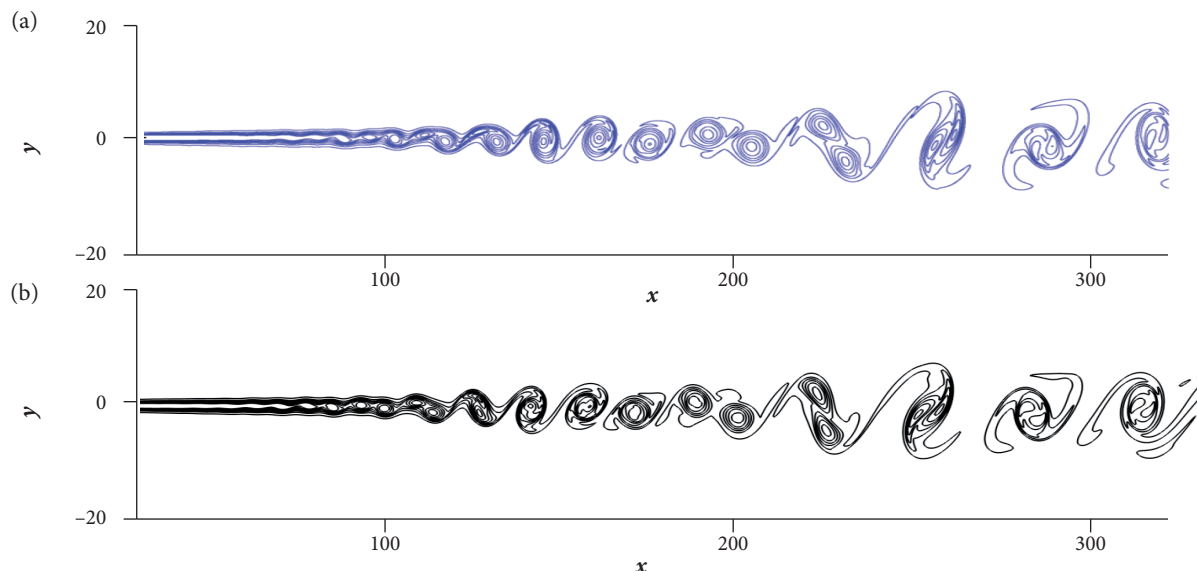


Figure 5. Spatial amplification rate in the streamwise direction. Comparison between LST and DNS for the 2D mixing layer.

Table 1. Spatial amplification rate comparison between DNS and LST for the 2D mixing layer.

x	(1,0)			(1/2,0)			(1/4,0)		
	LST	DNS	%	LST	DNS	%	LST	DNS	%
32	-0.108	-0.155	43	-0.086	-0.046	-46%	-0.05	0.0189	-138
37	-0.099	-0.093	-6	-0.084	-0.088	5%	-0.049	-0.042	-14
42	-0.092	-0.101	10	-0.081	-0.089	9%	-0.049	-0.052	5
47	-0.084	-0.085	1	-0.08	-0.081	1%	-0.049	-0.057	15
52	-0.078	-0.081	4	-0.078	-0.08	2%	-0.049	-0.054	10
57	-0.071	-0.073	3	-0.077	-0.083	8%	-0.049	-0.048	0
62	-0.065	-0.067	2	-0.075	-0.08	7%	-0.049	-0.051	5
67	-0.059	-0.059	1	-0.073	-0.079	9%	-0.048	-0.048	1

**Figure 6.** Spanwise vorticity contour levels from -0.26 up to 0.02 with an increment of 0.04 . Results from (a) Babucke *et al.* (2008) and (b) DNS code.

COMPRESSIBLE TWO-DIMENSIONAL PLANE JET

Plane jets are a typical shear flow present in several applications, such as in combustion and propulsion. There is also a fast growing interest in aerodynamic noise generated by jets in the aircraft industry. In this flow, a central core with high velocity mixes with a parallel stream with lower velocity. In the interface between both flow streams, there are high gradients of the flow properties, making the flow unstable to disturbances.

In the present investigation, a two-dimensional plane jet was studied. As in Reichert and Biringen (1997), the inflow velocity profile is:

$$u(y) = \frac{Ma_j - Ma_\infty}{Ma_j + Ma_\infty} \tanh(2y + \theta) + 1, \quad (22)$$

where $\theta = 1.98$ and the velocity profile is symmetrical with respect to $y = 0$, as shown in Fig. 7, and Ma_j and Ma_∞ are the Mach number in the core jet and in the far field, respectively. The ratio between the core jet velocity U_j and the far field co-flow velocity

U_∞ was $U_j/U_\infty = 1.67$ for all cases. The jet is perfectly expanded and isothermal such that the temperature, density and pressure profiles are kept constant. The adopted Prandtl number was $Pr = 0.71$. Since the DNS results are compared to inviscid linear stability analysis, the DNS simulations are done with a high Reynolds number ($Re = 10000$), thus the inertia effects are much higher than the viscous effects.

A computational Cartesian grid with 1400×800 nodes in x and y directions was used in all simulations. In the longitudinal direction, the grid is uniform with $\Delta x = 0.25$ up to $x \approx 250$ and then stretched at a 1.0% rate. In the normal direction, there is also a uniform grid with $\Delta y = 0.106$ up to $y \approx \pm 5.20$ and then stretched at a 1.0% rate. The uniform spacing zone corresponds to the interest zone, while the stretched grid region corresponds to the damping zone.

At the inflow, the undisturbed boundary conditions are given by Eq. 22 for the u velocity component and null for the v velocity component. The non-dimensional density and temperature are equal to one, and the total energy E is calculated by Eq. 2. As in the case of the two-dimensional mixing layer, the disturbances were introduced at each step of the Runge-Kutta method and the necessary care was taken to avoid numerical contamination of the solution.

The chosen time step was the same as the one previously considered $\Delta t = 2\pi/\omega \cdot n_{\text{steps}}$, where n_{steps} is the number of points per wavelength of the fundamental frequency. The number of time steps used for the fundamental frequency was $n_{\text{steps}} = 752$. In each case, 76 periods were simulated for the fundamental frequency, where the last eight were chosen for post-processing analysis.

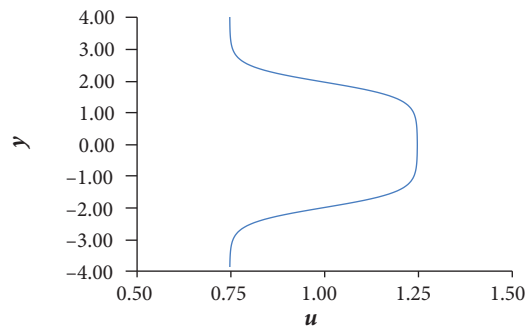


Figure 7. u velocity profile for the 2D plane jet.

An inviscid LST analysis was performed for each case, considering both sinuous and varicose modes. The simulated cases, their correspondent spatial amplification rate and frequency are presented in Tables 2 and 3, for sinuous and varicose modes, respectively. The frequencies were chosen close to the maximum amplification rate according to LST. The corresponding jet, free-stream and convective Mach numbers (Ma_j , Ma_∞ and Ma_c) are also shown in these tables. The convective Mach number is given by:

$$Ma_c = \frac{Ma_j - Ma_\infty}{2}. \quad (23)$$

Table 2. Mach numbers and spatial amplification rates of LST simulations. Sinuous mode.

Case	Ma_j	Ma_∞	Ma_c	ω_r	α_r	α_t
1	0.25	0.15	0.05	0.8859	0.8920	0.0966
2	1.05	0.63	0.21	0.8552	0.8616	0.0908
3	1.50	0.90	0.30	0.8199	0.8266	0.0849
4	2.00	1.20	0.40	0.7628	0.7699	0.0767
5	2.50	1.50	0.50	0.6862	0.6940	0.0674
6	3.00	1.80	0.60	0.5954	0.6038	0.0581

Table 3. Mach numbers and spatial amplification rates of LST simulations. Varicose mode.

Case	Ma_j	Ma_∞	Ma_c	ω_r	α_r	α_z
1	0.25	0.15	0.05	0.9036	0.8980	0.0933
2	1.05	0.63	0.21	0.8927	0.8875	0.0855
3	1.50	0.90	0.30	0.8740	0.8690	0.0773
4	2.00	1.20	0.40	0.8350	0.8301	0.0654
5	2.50	1.50	0.50	0.7636	0.7586	0.0507
6	3.00	1.80	0.60	0.6370	0.6311	0.0335

The variation of the spatial amplification rate with Ma_j is shown for the sinuous mode in Fig. 8 and for the varicose mode in Fig. 9. Increasing the Mach number, there is a decrease in the amplification rate value, and the flow becomes more stable. The varicose mode is more sensitive to compressibility effects and the growth rates decay faster with increasing Mach numbers.

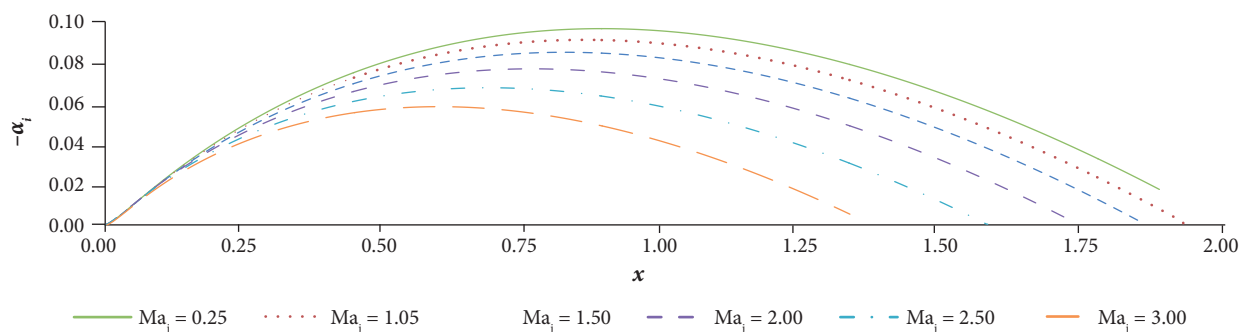


Figure 8. Spatial amplification rates for the 2D plane jet, sinuous mode.

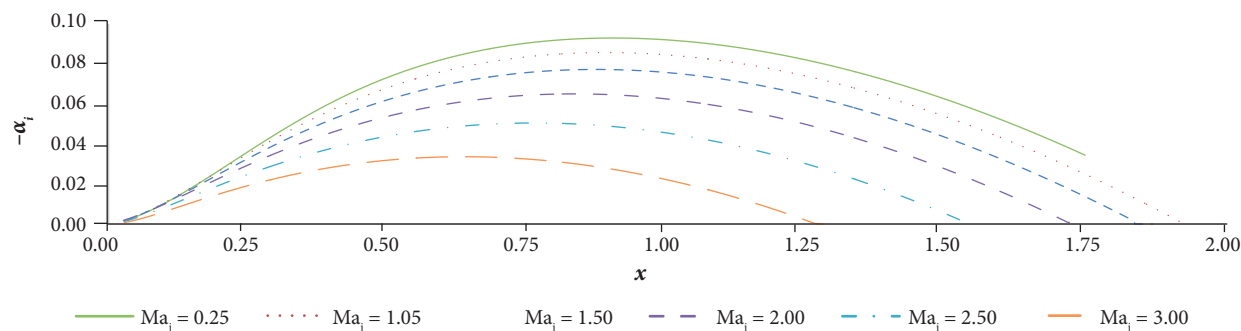


Figure 9. Spatial amplification rates for the 2D plane jet, varicose mode.

The decrease of the amplification rate with compressibility and consequent mixing of the flow is a known effect. This effect is of great importance in combustion flows and can help in noise control. Figures 10 and 11 show the spanwise vorticity for the sinuous and varicose modes, where the vortex generation pattern is anti-symmetrical for the sinuous mode and symmetrical for the varicose mode. For both modes, increasing the Mach number is followed by an increase in the undisturbed jet core length and a lower spreading of the vorticity thickness, since the flow is more stable as predicted by the LST analysis.

The maximum amplitude of the normal velocity v along the y direction, as a function of the streamwise x position ($|v|_{max}$), is presented in Fig. 12 for the sinuous mode, and in Fig. 13 for the varicose mode. An initial receptivity region can be noticed

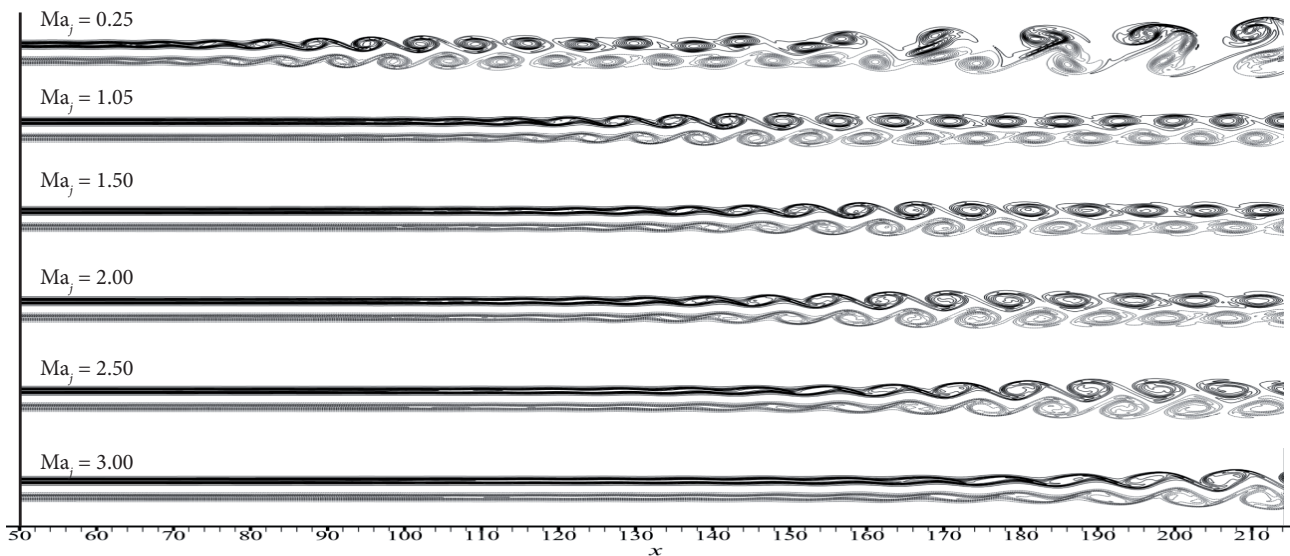


Figure 10. Spanwise vorticity for the 2D plane jet, sinuous mode. Contour levels from -0.5 to 0.5 . Solid lines for positive values and dashed lines for negative values.

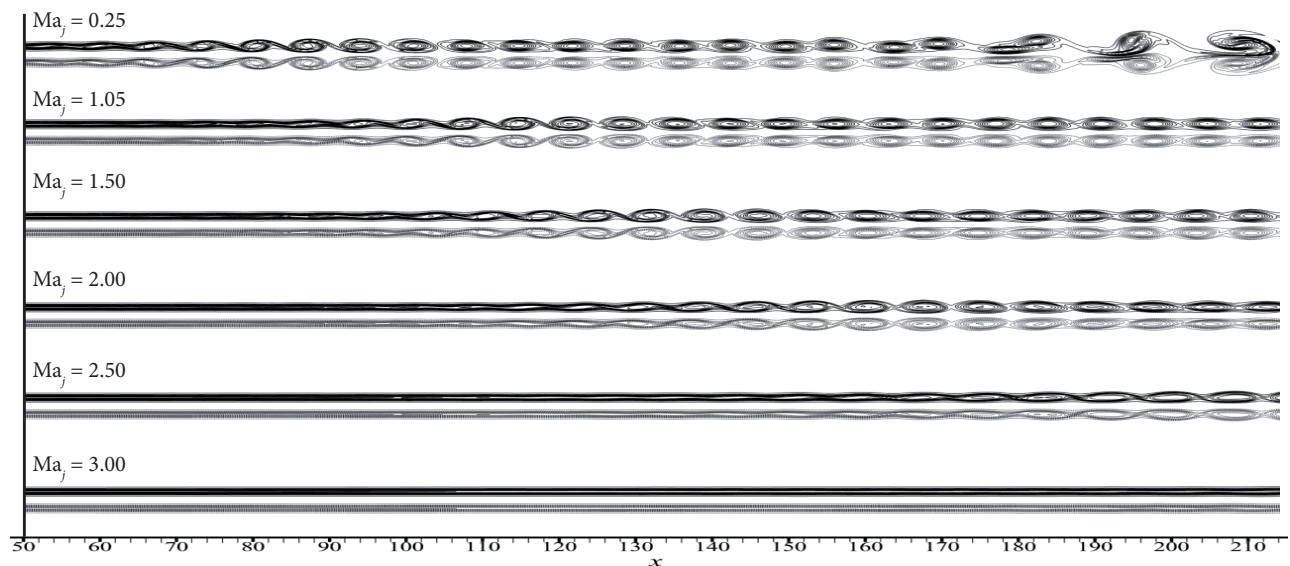


Figure 11. Spanwise vorticity for the 2D plane jet, varicose mode. Contour levels from -0.5 to 0.5 . Solid lines for positive values and dashed lines for negative values.

near the inflow. The length of this region depends on the Mach number and the case, sinuous or varicose. Further downstream, disturbances grow exponentially, corresponding to linear growth. In this region, it is possible to compare the amplification rates obtained with DNS and LST. For instance, for the sinuous mode and $Ma_j = 0.25$, this region is approximately from $x = 15.0$ up to $x = 60.0$ while, for $Ma_j = 1.50$, this region is approximately from $x = 50.0$ up to $x = 150.0$. As the flow becomes more stable with increasing Mach number, the x position where the disturbances grow exponentially is delayed to a position further downstream. After the linear growth region, there is a region where the non-linear effects starts to become significant, where the LST theory is no longer valid.

Since DNS results have these three distinct regions, where the linear region may be contaminated by the overlap of the initial transient and the nonlinear regions, it was decided to compare the maximum amplitude of the normal velocity with the amplitude

predicted by the LST theory, instead of the amplification rates. A good agreement was observed between LST and DNS results and this can be used to consider the DNS code verified.

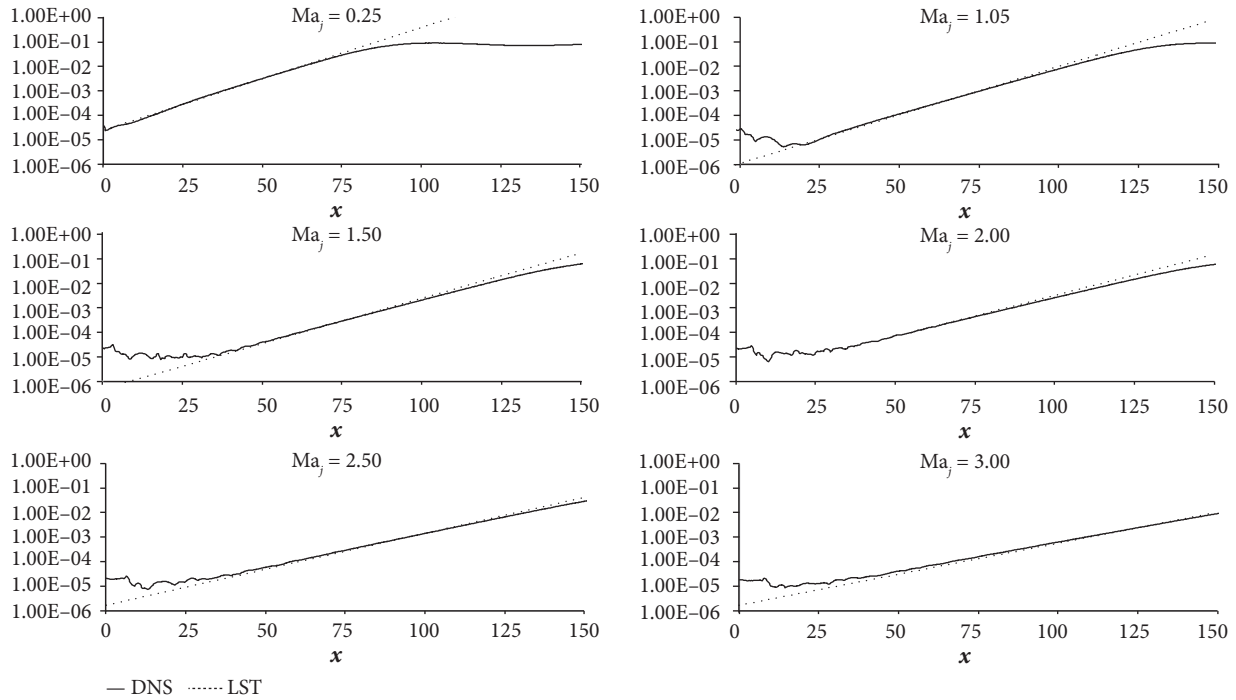


Figure 12. Maximum streamwise amplitude variation of the normal velocity component for sinuous mode.

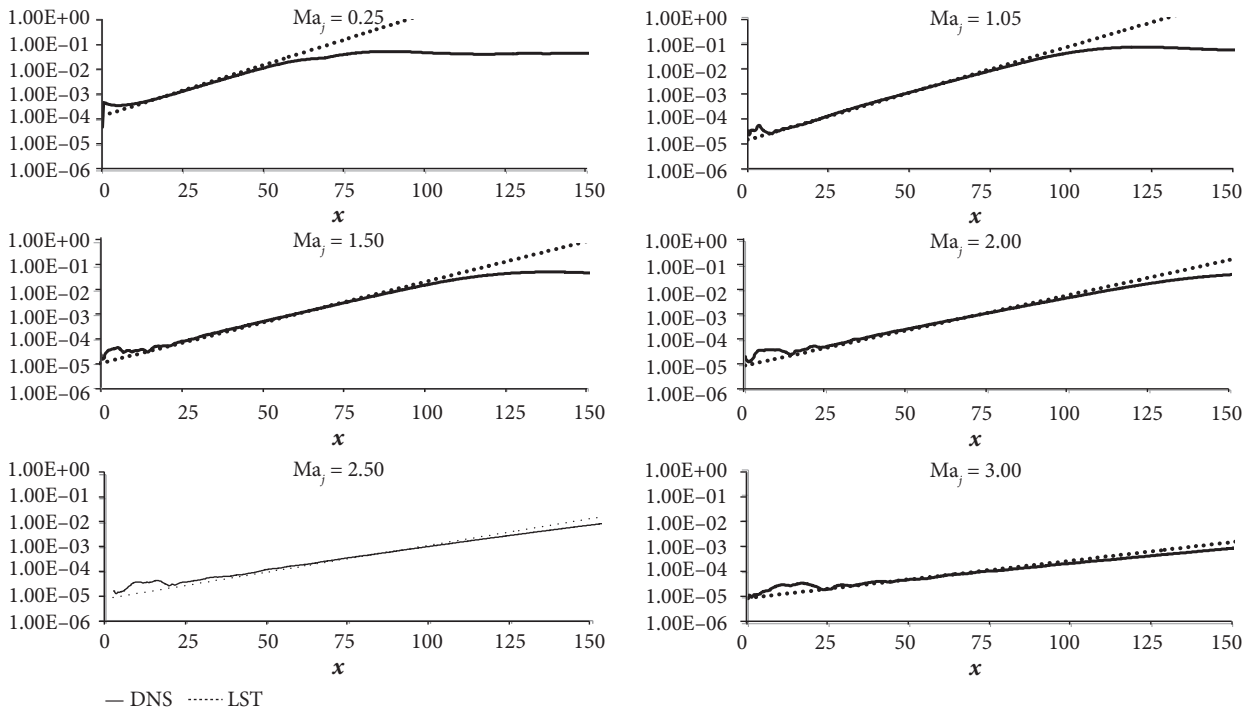


Figure 13. Maximum streamwise amplitude variation of the normal velocity component for the varicose mode.

SUMMARY

Two compressible shear flows were simulated using a two-dimensional DNS code, a two-dimensional compressible mixing layer and a two-dimensional compressible plane jet. For the mixing layer the results were compared with LST and the results available in the literature. For the plane jet, comparisons were presented between the DNS results and the linear stability theory. Very good agreement was found in regions where LST predictions are valid. The DNS code was able to correctly recover growth rates for different disturbance frequencies and convective Mach numbers ranging from 0.05 to 0.6 (corresponding to jet Mach numbers from 0.25 up to 3). The study shows that DNS code is a valid tool to investigate disturbance propagation on compressible flows if proper care is taken to avoid wave reflections from the boundaries and if a low dissipation and low dispersion numerical scheme is used.

AUTHOR'S CONTRIBUTION

Conceptualization, Lacerda JF and Souza LF; Methodology, Souza LF and Mendonça MT; Investigation, Lacerda JF and Rogenski JK; Writing – Original Draft, Lacerda JF; Writing – Review & Editing, Lacerda JF; Souza LF; Rogenski JK and Mendonça MT.

REFERENCES

- Babucke A, Kloker M, Rist U (2008) DNS of a plane mixing layer for the investigation of sound generation mechanisms. *Comput Fluids* 37(4):360-368. doi: 10.1016/j.compfluid.2007.02.002
- Curle N (1955) The influence of solid boundaries upon aerodynamic sound. *Proceedings of the Royal Society of London. Series A. Mathematical and Physical Sciences* 213(1187):505-514. doi: 10.1098/rspa.1955.0191
- Ffowcs-Williams JE, Hawkings DL (1969) Sound generation by turbulence and surfaces in arbitrary motion. *Philosophical Transactions of the Royal Society of London. Series A. Mathematical and Physical Sciences* 264(1151):321-342. doi: 10.1098/rsta.1969.0031
- Lighthill MJ (1952) On sound generated aerodynamically. I. General theory. *Proceedings of the Royal Society of London. Series A. Mathematical and Physical Sciences* 211(1107):564-587. doi: 10.1098/rspa.1952.0060
- Lighthill MJ (1954) On sound generated aerodynamically. II. Turbulence as a source of sound. *Proceedings of the Royal Society of London. Series A. Mathematical and Physical Sciences* 222(1148):1-32. doi: 10.1098/rspa.1954.0049
- Reichert R, Biringen S (1997) Numerical simulation of compressible plane jets. *AIAA* 28:1-15. doi: 10.2514/6.1997-1924
- Souza LF, Mendonça MT, Medeiros MAF (2005) The advantages of using high-order finite differences schemes in laminar-turbulent transition studies. *Int J Numer Methods Fluids* 48:565-592. doi: 10.1002/flid.955
- Tam CKW (2004) Computational aeroacoustics: an overview of computational challenges and applications. *Int J Comput Fluid D* 18(6):547-567. doi: 10.1080/10618560410001673551